



Seismic tomography of the uppermost inner core

Scott Burdick^{a,*}, Lauren Waszek^{b,c}, Vedran Lekić^d

^a Department of Geology, Wayne State University, Detroit, MI, United States

^b Department of Physics, New Mexico State University, Las Cruces, NM 88001, United States

^c Research School of Earth Sciences, Australian National University, Acton, ACT 2601, Australia

^d Department of Geology, University of Maryland, College Park, United States

ARTICLE INFO

Article history:

Received 5 December 2018

Received in revised form 3 July 2019

Accepted 23 August 2019

Available online 19 September 2019

Editor: B. Buffett

Keywords:

inner core

tomography

Bayesian inference

ABSTRACT

Seismic body wave and normal mode analyses have revealed that the inner core is solid, strongly anisotropic, and characterized by dramatic quasi-hemispherical differences in elastic structure and attenuation. Yet, despite these discoveries, the highly heterogeneous and incomplete data coverage of the inner core has impeded the development of tomographic models even at the longest wavelengths. Here, we use a probabilistic and transdimensional tomographic approach (TBI) on a newly expanded dataset of P-wave travel-times sensitive to the upper 120 km of the inner core. The TBI approach yields an ensemble of parsimonious models that simultaneously capture both the dominant hemispheric dichotomy and laterally abrupt velocity variations. Analysis of the model ensemble allows us to determine the locations of the hemisphere boundaries and rule out the presence of hemispheric dichotomy in anisotropy. Instead, we robustly map regional variations in anisotropy beneath Africa and the eastern Pacific, and detect variations at high latitudes suggesting that cylindrical anisotropy may not be adequate for describing the uppermost inner core.

© 2019 Elsevier B.V. All rights reserved.

1. Introduction

The structure of Earth's inner core has wide-ranging implications for our understanding of Earth's thermal history, core dynamics, and magnetic field generation. Its seismic characteristics inform us about its composition (Antonangeli et al., 2010; Geballe et al., 2013; Romanowicz et al., 2016) and bear the signature of the dynamical mechanisms of formation and evolution (Aubert et al., 2008; Monnereau et al., 2010; Alboussière et al., 2010; Lasbleis et al., 2017). Inner core seismic velocity structure is dominated by a distinct hemispherical dichotomy, comprising a slow west hemisphere, and a fast east hemisphere (e.g. Tanaka and Hamaguchi, 1997; Niu and Wen, 2001; Cao and Romanowicz, 2004; Deuss et al., 2010; Waszek et al., 2011). Cylindrical velocity anisotropy is observed to be oriented with the fast direction aligned to Earth's rotation axis (Morelli et al., 1986; Woodhouse et al., 1986; Creager, 1992), stronger in the western hemisphere, and with complex radial variation (Song and Helmberger, 1995; Creager, 1999; Deuss et al., 2010; Waszek and Deuss, 2011). The properties of these characteristics are debated, and unanswered questions re-

main regarding regional velocity variations, strength of anisotropy, relationship between velocity and attenuation, and location and sharpness of hemisphere boundaries (Tkalčić, 2015). As a result, detailed observational studies are essential to orient future geodynamic and mineral physics work (Lasbleis et al., 2017).

Most seismic studies of the inner core concern themselves with describing the hemispheric dichotomy, which represents a spherical harmonic degree-one structure. Reported differences between the hemispheres for isotropic velocity range between 0.5 and 1.5% in V_p (Tanaka and Hamaguchi, 1997; Niu and Wen, 2001; Waszek and Deuss, 2011), although a recent study argued that this hemispheric isotropic difference can be attributed to anisotropic variations in certain regions (Irving and Deuss, 2015). Lateral variations in the strength of anisotropy are also usually discussed by hemisphere. The western hemisphere displays a 50–100 km thick isotropic upper layer (Garcia and Souriau, 2000; Waszek and Deuss, 2011); beneath, anisotropy increases radially, from values of around 3% potentially up to 8% at greater depths (Song and Helmberger, 1995; Irving and Deuss, 2011). In contrast, the eastern hemisphere is negligibly anisotropic (less than 0.5%) (Niu and Wen, 2001; Yu and Wen, 2007). Regional variations in properties combined with different sampling geometries may explain much of the deviations between studies.

The location and sharpness of boundaries between the two hemispheres have been used to place limits on inner core super-

* Corresponding author.

E-mail address: sburdick@wayne.edu (S. Burdick).

URL: <https://clasprofiles.wayne.edu/profile/gm8759> (S. Burdick).

rotation (e.g. Waszek et al., 2011) and convection (e.g. Geballe et al., 2013). The boundaries are situated approximately beneath Africa and the Pacific Ocean; estimates of their locations vary from 10–60° and 150–180° (e.g. Tanaka and Hamaguchi, 1997; Creager, 1999; Garcia and Souriau, 2000; Niu and Wen, 2001; Yu and Wen, 2007; Irving and Deuss, 2011). Recent body wave studies agree that they are relatively sharp, on the order of hundreds of kilometers (Waszek et al., 2011; Irving and Deuss, 2015; Yu et al., 2017; Godwin et al., 2018). The disagreement in location may be attributed to paucity of data sampling (Tkalcic, 2015), or radial and/or lateral variation (Deuss et al., 2010; Irving and Deuss, 2011; Irving, 2016; Yu et al., 2017; Godwin et al., 2018).

The strongest observational evidence for consistent regional structure within the hemispheres comes from normal mode studies, since they provide global coverage, albeit at low resolution. Deuss et al. (2010) reported significant variation in anisotropy around a hemispherical average. Regional body wave studies agree, finding localized features beneath the Pacific Ocean (Cormier et al., 2011; Irving and Deuss, 2015; Yu et al., 2017; Godwin et al., 2018), as well as beneath Africa (Yu and Wen, 2007; Irving, 2016), and Central America (Blom et al., 2015). However, some of the strong regional anisotropy inferred from body wave data has been attributed to unmodeled effects from the lowermost mantle, particularly beneath the middle western hemisphere (Tkalcic, 2015).

There are two primary hypotheses to explain the inner core hemispherical structure. In the first, hemispheres are frozen into the inner core structure as it solidifies from the liquid outer core. The hemispheres are generated by an asymmetry in heat loss and thus freezing rates (Aubert et al., 2008), resulting from thermochemical coupling of the inner core to the core-mantle boundary. Higher heat flux in the eastern hemisphere produces faster solidification, and the resultant difference in crystal size and orientation accounts for the seismic properties. The second hypothesis invokes degree one convection to generate the hemispheric dichotomy: a lateral translation eastward, driven by melting of the east hemisphere and freezing in the west (Alboussiere et al., 2010; Monnereau et al., 2010). This produces a hemispherical difference in material age, whereby the east hemisphere is older. Age is correlated to domain size of crystals (Bergman et al., 2010), and seismic properties (Geballe et al., 2013). Note that recent estimates of inner core conductivity may preclude this convective mode (Pozzo et al., 2012), although it may be driven compositionally (Deguen et al., 2013).

Both hypotheses have difficulty explaining the seismic properties beyond the basic east-west dichotomy. In particular, the presence of laterally and radially varying anisotropy has not been incorporated into geodynamical models. The models struggle to explain the sharp transition in seismic properties at the boundaries; Geballe et al. (2013) found that sufficiently abrupt boundaries may be generated by inner core translation only for very specific mineral compositions. Regional-scale variations in velocity, which are suggested to arise from lateral discrepancies in heat flux across the inner core boundary (Gubbins et al., 2011), are not explicitly modeled. The fundamental issue impeding the study of small-scale variations is that seismic constraints are poor (Lasbleis et al., 2017). Higher-resolution seismic models are therefore crucial for motivating and testing geodynamical simulations.

In this study we use a large dataset of *PKiKP*–*PKIKP* differential travel times (Waszek and Deuss, 2013) to constrain heterogeneity in the uppermost inner core. *PKIKP* traverses the uppermost ~100 km of the inner core, and is measured against the reference phase *PKiKP*, which reflects from the inner core boundary. Although this is a common technique to explore the seismic properties of the uppermost inner core (e.g. Niu and Wen, 2001; Cao and Romanowicz, 2004; Waszek et al., 2011), numerous potential complications in the geometry of this problem can intro-

duce trade-offs between regional isotropic variations, anisotropy, and heterogeneity in the mantle and outer core.

First, *PKiKP* paths sampling the upper inner core have a narrow range of epicentral distances (~130–143°), limiting the potential number of data. In particular, the polar regions are poorly instrumented and have few earthquakes suitable for inner core studies, leading to few polar paths. Second, the sparsity of paths, combined with the short distance that the *PKIKP* phase travels through the upper inner core (<30°) means that few regions are covered by crossing and overlapping paths. Finally, although *PKiKP* and *PKIKP* take similar paths through the bulk of the mantle, it is possible that strong, small-scale heterogeneity in the *D* region, and lateral velocity variations in the uppermost and lowermost outer core may introduce errors, a significant problem considering the small differential *PKiKP*–*PKIKP* time (1–2 s) accumulated in the inner core.

These difficulties have hindered efforts to recover inner core structure with standard approaches to seismic tomography. Inverting only for hemispheres or fixed large-scale grids can underestimate regional heterogeneity or misplace major boundaries, while damped least-squares inversions run the risk of over-fitting spatially biased data or smearing out sharp gradients. By employing an adaptive parameterization and avoiding damping, Transdimensional Bayesian Inference (TBI) (e.g. Burdick and Lekic, 2017) offers one potential way to circumvent these issues.

Recent TBI developments have focused on using reversible-jump Markov Chain Monte Carlo (Green, 1995; Sambridge et al., 2006) to estimate the posterior probability of geophysical properties. Chains of models are created by varying one parameter at a time. Each new model is accepted or rejected based on how well it fits the data and prior information, and, after a sufficient number of iterations, models appear in the chain proportional to their probability. Application to global and teleseismic problems have featured applications to surface wave tomography (e.g. Bodin and Sambridge, 2009; Bodin et al., 2012; Oluogboji et al., 2017) and receiver function surveys (e.g. Agostinetti and Malinverno, 2010). Due to the more computationally demanding forward problem, body wave applications have been more limited, and recent studies have focused on local earthquake tomography (Piana Agostinetti et al., 2015) or on recovering a single layer of heterogeneity (Young et al., 2013; Tkalcic et al., 2015). By performing forward computations on an underlying unchanging grid, Burdick and Lekic (2017) recently applied TBI to continent-scale tomography in three spatial dimensions.

Regardless of application, TBI methods offer three primary advantages over traditional approaches. First, they yield an ensemble of models which can be analyzed to quantify model uncertainty and trade-offs between parameters. Second, they estimate the variance of data errors alongside the geophysical properties, enabling optimal weights across different data types (Bodin et al., 2012). Third, the number, position, and geometry of parameters is allowed to vary ensuring flexible yet parsimonious parameterization (Malinverno, 2002). These aspects render the TBI approach well-suited to the problem of inner core tomography—flexibility in the position and orientation of model domains allows for the estimation of hemisphere boundary locations, and the parsimonious parameterization ensures that sub-hemispheric variations are inserted only where necessary.

In this study, we extend the method of Burdick and Lekic (2017) to constrain isotropic and anisotropic *P*-wave velocities in the uppermost 120 km of the inner core with *PKiKP*–*PKIKP* differential travel times. From the ensemble models, we are able to estimate hemispheric and regional compressional velocity (V_P) variations and their uncertainty, the trade-off between isotropic V_P and cylindrical anisotropy, and location uncertainty of the hemispheric boundaries beneath Africa and the Pacific. In order to quantify the

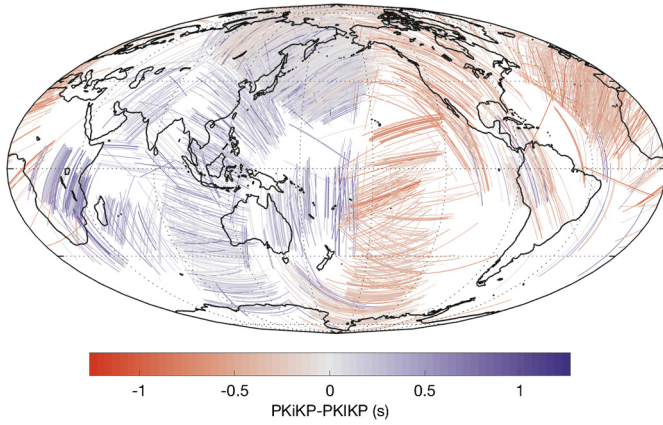


Fig. 1. Map of inner core paths of *PKiKP* phases used in this study. Color shows *PKiKP*–*PKiKP* differential travel time residuals, calculated with respect to AK135. Blue indicates a faster travel through the inner core.

contribution of mantle heterogeneity, we also compare inner core models based on ray paths and differential travel times calculated in several different Earth models.

2. Methodology

2.1. Data and processing

Our study benefits from a large dataset of *PKiKP*–*PKiKP* differential travel time residuals (Waszek and Deuss, 2013), augmented with additional residuals from events up to May 2016. We choose station–event pairs with epicentral distances between 129° and 144° degrees, for which *PKiKP* turns within the upper 120 km of the inner core. The data were measured using cross-correlation and hand-picking techniques at corner frequencies of 0.7 – 2.0 Hz and compared to theoretical travel times derived from AK135 (Kennett et al., 1995). A detailed description of the processing and picking methods may be found in Waszek et al. (2011), Waszek and Deuss (2011). The full dataset of 5075 differential travel time residuals is shown in Fig. 1, projected onto their respective *PKiKP* paths through the inner core.

Data coverage is clearly dominated by a high density of stations in the northern hemisphere, especially the US. Large swaths of the Southern hemisphere are sparsely sampled, and ray paths are almost completely absent in the South Atlantic, as pointed out by Pejić et al. (2017). Due to the geometry of *PKiKP* in our chosen range, rays travel almost entirely in the equatorial direction near the poles (e.g. Tkalcic et al., 2015), which will lead to a high degree of uncertainty in anisotropy away from the equator.

2.2. Tomographic problem

The tomography method we use in this study is two-fold. In this section, we describe the forward problem relating the anisotropic variations in inner core velocity to differential travel times, and in the following section we describe the solution to the inverse problem using Transdimensional Bayesian Inference.

For each station–event pair, we trace *PKiKP* and *PKiKP* ray-paths through the inner core and compute the expected differential travel time, dT . In order to estimate the potential effects of 3D mantle heterogeneity on the differential travel times, we calculate rays and travel times in three mantle tomographic models—the 1D reference Earth model AK135, and two 3D P-wave models, ME2016 (Moulik and Ekstrom, 2016) and LLNL-G3Dv3 (Simmons et al., 2012). Ray tracing was performed with the TauP toolkit (Crotwell et al., 1999) for AK135 and with LLNL-Earth3D (Simmons et al., 2012) for the 3D models.

We seek models of anisotropic V_P that minimize the difference between the observed differential travel times and those predicted by the reference Earth model:

$$\Delta T = dT_{obs} - dT_{pred}. \quad (1)$$

We follow Burdick and Lekić (2017) and define our forward problem on a static underlying model grid with dimensions $0.7^\circ \times 0.7^\circ \times 120$ km in depth. This parameterization is appropriate for our dataset, since it is not suited for mapping the depth-dependence of seismic properties within the inner core. Within each of the grid volumes, the length of each ray is calculated. As we wish to test the hypothesis that the inner core is anisotropic with the fast axis aligned with the Earth’s rotational axis (hereafter referred to as axial anisotropy), we also retain the angle ζ between each ray segment and the rotational axis.

Finally, we follow Creager (1999) and set up a linear forward problem relating residual travel times to the anisotropic V_P in each grid volume:

$$\frac{\Delta T}{T} = \frac{dV_P}{V_P} + b \cos^2 \zeta + c \cos^4 \zeta, \quad (2)$$

where dV_P is P -wave velocity perturbation, V_P is the mean layer velocity, and b and c are two terms describing axial anisotropy. The total anisotropy, $b + c$ represents the difference in velocity between waves traveling along axial and equatorial paths. A positive value for $b + c$ indicates that waves travel faster in the direction of the rotational axis. For clarity, we report model values as percent perturbation in P -wave velocity ($\% dV_P/V_P$).

To confirm the accuracy of our forward problem and provide a point of comparison with the TBI results, we performed a damped least squares inversion of the residual travel times relative to AK135. The resulting model is shown in the Supplementary Materials (Fig. S1).

2.3. Transdimensional Bayesian inference

Motivated by the sparse and uneven coverage of inner core ray paths and the desire to, where possible, constrain regional structure in addition to average properties of the hemispheres, we apply Transdimensional Bayesian Inference to the inner core tomography problem. Bayes’ Theorem states that the posterior probability assigned to a model is proportional to the likelihood that model explains the observed data and the extent to which it agrees with all prior information. We seek to estimate the posterior probability distribution of anisotropic models given the *PKiKP* – *PKiKP* travel time dataset.

We proceed by applying a reversible-jump Markov chain Monte Carlo algorithm (Green, 1995) to generate an ensemble of models sampling the posterior distribution. Each starting model is parameterized based on three sets of randomized Voronoi nuclei (Okabe et al., 1992), one for each velocity term (V_P , b , and c). Using independent sets of parameters can be advantageous when one term (in our case, V_P) is much better constrained than the others (Gao and Lekic, 2018). We cluster together underlying grid volumes into parameters of constant value according to their nearest Voronoi nucleus. Fig. 2 shows a schematic of our approach. Differential travel times predicted by each model can then be calculated by computationally fast matrix multiplication.

The models are randomly updated in succession by changing one Voronoi nucleus at a time. At each step, a new model is proposed based on one of four operations:

1. Change velocity assigned to a Voronoi nucleus by an amount drawn from normal distribution about its current value ($\sigma = 0.14\% dV_P/V_P$).

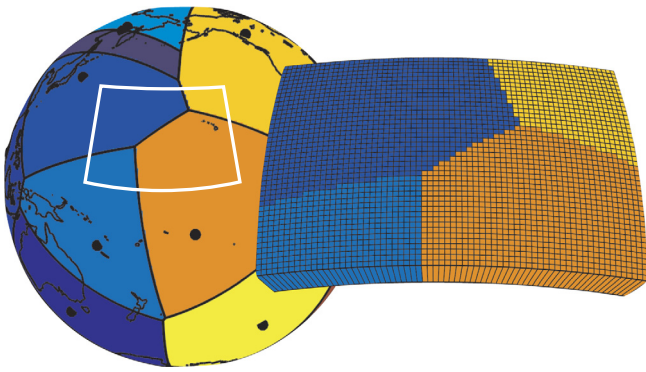


Fig. 2. An overview of the model parameterization. Left: The inner core is split up into a set of Voronoi cells defined by nuclei (black dots). Right: Underlying $0.7^\circ \times 0.7^\circ \times 120$ km grid volumes on which sensitivity kernels are defined are clustered together according to nearest nuclei.

2. Move one nucleus along a great circle path in random direction. The distance is drawn from a normal distribution ($\sigma = 120$ km).
3. Add a new nucleus in a random location with velocity value drawn from the prior.
4. Remove a nucleus.

Once proposed, each new model is accepted or rejected based on how much more probable it is than the last according to the Metropolis Hastings algorithm (Metropolis et al., 1953). The probability here depends on how well the predicted data fits the observed data, how well the model agrees with the prior, and the number of Voronoi volumes used. In this study, the velocity values for new volumes are drawn from the prior, a normal distribution about zero with $\sigma = 1.4\% dV_p/V_p$. We choose our prior to be in line with previous body wave and normal mode studies of the outermost inner core. For this approach, the acceptance criteria for increasing or decreasing the number of cells simplify to $(N+1)/N$ for removing a cell and $(N+1)/(N+2)$ for adding a cell (Kolb and Lekić, 2014).

Each model undergoes a chain of updates, and, after a burn-in period during which the models depend on their starting value, the current model is saved to an ensemble solution at regular intervals. At the end of the process, the frequency with which a model value appears in the ensemble is proportional to its posterior probability. From the ensemble we obtain a probability density function (pdf) from which statistical values—like the mean and standard deviation of velocity, as well as the probability that a location contains a hemispheric boundary—can be derived.

2.4. Background assumptions

It is vital to note that the posterior probability distributions we find in this study and the conclusions drawn from them are dependent on a set of background assumptions. To some extent, each of these assumptions is commonly held in body wave studies of the inner core. The merits of some of the assumptions are discussed below, and the rest will serve as the basis for future study.

First, we assume that the data errors can be considered independent and normally distributed. Since the residual travel times are determined by cross-correlation, the data error may admit to a more complicated formulation. We also assume that the sensitivity of the differential travel times to inner core structure to *PKIKP* can be adequately represented by ray theory, i.e. finite frequency effects are minimal. Second, with respect to parameterization, we assume that the underlying grid is adequate to recover the scale of heterogeneity and location of hemispheric boundaries. We assume that heterogeneity in the top 120 km of the inner core can be

modeled as a single layer. While this may represent an oversimplification, it is dictated by limited data coverage, and is consistent with other regional inner core studies (Irving and Deuss, 2015; Irving, 2016). We also assume that anisotropy is cylindrical with the c-axis aligned with the Earth's rotational axis. Finally, although we attempt to test the effect of velocity variations in the mantle, we make assumptions about other outside effects on the observations. We assume that the mantle models we test adequately represent the scale and strength of mantle heterogeneity, in particular near the core-mantle boundary (CMB). Furthermore, we assume that neither potential outer core heterogeneity nor topography on the CMB and inner core boundary (ICB) affect the differential travel times.

3. Results

3.1. Quasi-hemispheric TBI model

For an initial TBI inversion, we constrain each term of anisotropic velocity to two quasi-hemispheres with constant velocity apiece and allow the longitude of the two boundaries and velocity within the hemispheres to vary. For this inversion, data residuals are recomputed relative to LLNL-G3Dv3. We run 10 chains for one million iterations each, saving every 100th model after a burn-in period of 10,000 iterations. The resulting mean model and uncertainty are shown in Fig. 3.

The location and isotropic velocities of the hemispheres (Fig. 3a) are well-constrained, with mean values of 0.35% dV/V in the eastern hemisphere and -0.7% dV/V in the western. Fig. 3c shows the standard deviation of the isotropic model. Within each hemisphere, the standard deviation of the isotropic model is $\sim 0.1\%$ dV/V , but increases up to 0.5% dV/V at the hemisphere boundaries. This high standard deviation is likely due to uncertainty in the location of the boundaries (e.g. Burdick and Lekić, 2017; Olugboji et al., 2017). Since the boundaries of quasi-hemispheres are allowed to move around, leading to a bimodal posterior distribution and a larger error bar. Here, we estimate that the Pacific boundary is at $192^\circ \pm 3^\circ$. The African side is more uncertain, with the boundaries falling between 5° – 28° and a peak value at 24° .

In contrast, there is no agreement on the location of the anisotropic hemispheres (Fig. 3b). Although the mean model places $b+c$ between 0.4 and 0.55% dV/V at all longitudes, the location of the boundaries varies greatly in the ensemble, defining hemispheres with no relation to those in the isotropic part, often of mismatched size. The standard deviation of $b+c$ (Fig. 3d) is higher than the isotropic part, ranging from 0.15 beneath the Pacific to 0.4 beneath the Atlantic and Africa. The higher values are likely due to disagreement over the location of the hemispheres and lack of ray paths constraining anisotropy in the region. Taken together, these results suggest that a quasi-hemispheric model is inadequate for describing the lateral variations of inner core anisotropy.

3.2. 2D TBI model

We allow the number and location of the model parameters to vary and represent lateral variations of inner core structure. We cap at 100 the number of possible Voronoi nuclei for each type of model parameter. The positions of the nuclei were allowed to vary from 120 km below the ICB to 500 km above, which we found to be an efficient way to define smaller-scale regions within our model domain.

We performed equivalent inversions for residuals calculated in each of the three reference models. For each ensemble, we ran 60 rj-MCMC chains for 500,000 iterations. After a burn-in period of 50,000 iterations – after which the statistical properties of the chains appeared to converge – we saved every 100th model to an

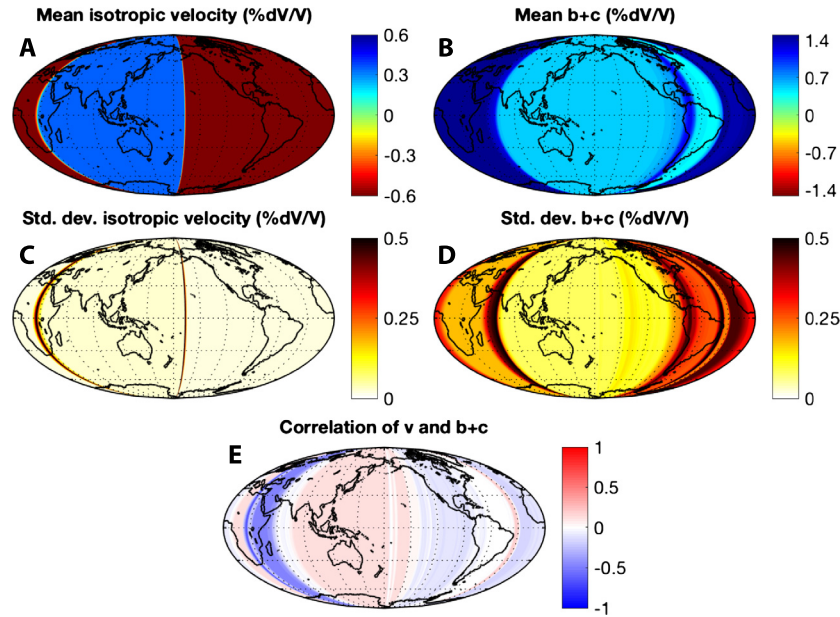


Fig. 3. Summary of TBI model ensemble with anisotropic quasi-hemispheres. (a) Mean isotropic V_p . (b) Standard deviation of isotropic V_p . (c) Mean $b + c$ anisotropy. (d) Standard deviation of $b + c$ terms. (e) Posterior correlation between lateral variations of isotropic V_p and $b + c$.

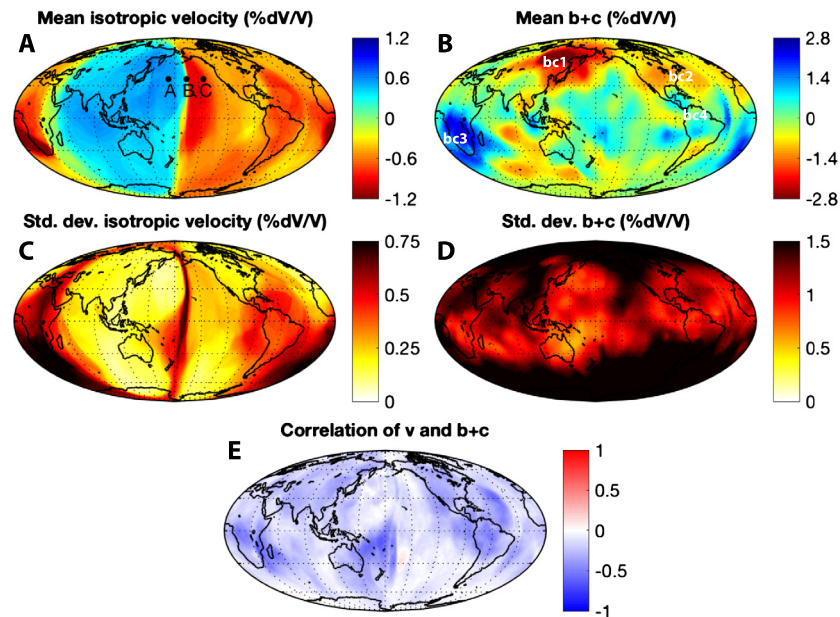


Fig. 4. Summary of TBI model ensemble. (a) Mean isotropic V_p . (b) Standard deviation of isotropic V_p . (c) Mean $b + c$ anisotropy. (d) Standard deviation of $b + c$. (e) Posterior correlation between lateral variations in isotropic V_p and $b + c$. Labeled points in (a) give the location of histograms in Fig. 6.

ensemble, for a total of 27,000 models per ensemble. In each inversion, the algorithm fit the isotropic part of the velocity with ~ 20 Voronoi cells, while the b and c , which demonstrate stronger regional variation were fit with ~ 100 parameters each. In this section, we present our preferred inner core model, which uses data residuals calculated using the LLNL-G3Dv3 mantle model. We prefer this result because the 3D mantle corrections and final inner core model display the greatest variance reduction of the three. A full comparison of the results can be found in Section 4.1.

The resulting preferred model properties are shown in Fig. 4. The mean isotropic model (Fig. 4a) exhibits clear isotropic hemispheres, with average values of 0.4% dV/V in the eastern hemisphere and -0.6% dV/V in the western hemisphere. Regional variations are more prevalent in the western hemisphere, with local low velocities adjacent to the hemispheric boundaries and beneath

the central Atlantic. Resolution tests (see Supplementary Materials, Figs. S6, S8) indicate that the data are capable of constraining intra-hemispheric variations of this scale and amplitude. The uncertainty in isotropic variations (as defined by the standard deviation of the ensemble models) is $\sim 0.15\%$ dV/V in the well determined areas of the hemispheres ranging up to 0.2% dV/V in parts of the eastern hemisphere. Beneath the southern Atlantic the uncertainty reaches a maximum of 0.75% dV/V and moderate uncertainty (0.4–0.5) arises beneath South America. It is unlikely that isotropic variations can be trusted in these regions. To better assess the significance of velocity variations compared to the model uncertainty, Fig. 5 shows cross-sections through the model probability density function at constant latitudes.

High posterior uncertainties also appear at the edges of the hemispheres due to uncertainty in boundary location. Ambiguity

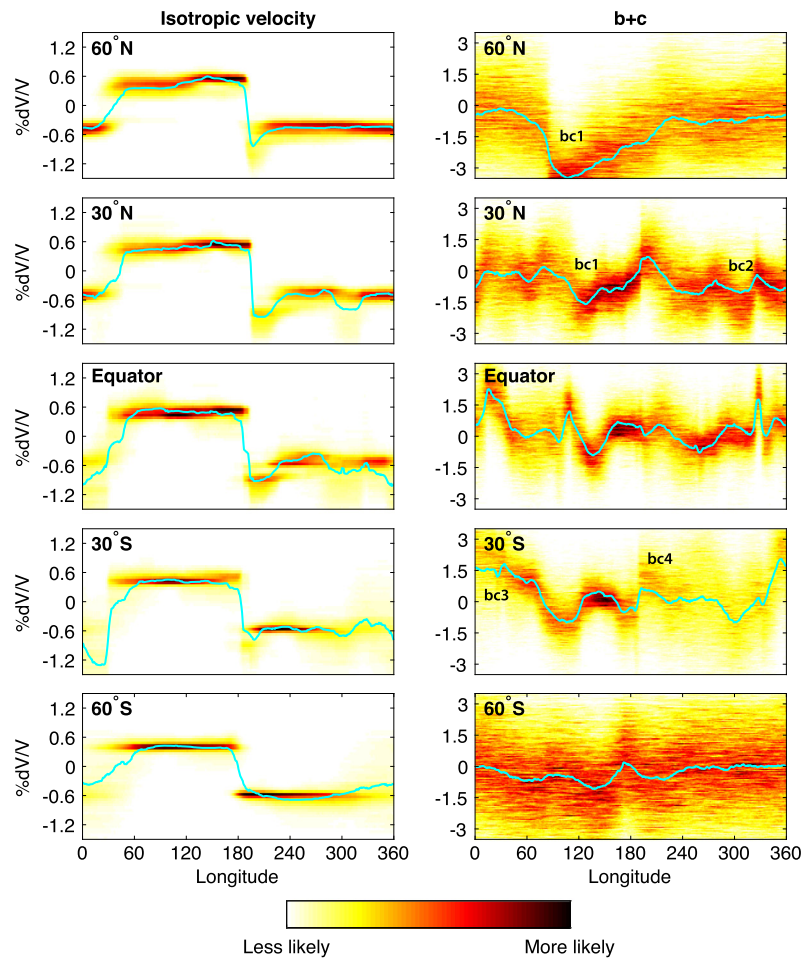


Fig. 5. Probability density functions for isotropic velocity (left) and $b + c$ (right) along constant latitude slices. Note the different scaling in velocity value. Locations for the slices are indicated by grid lines in Fig. 4. The mean model values are given by the cyan lines. Colors show relative probability, with darker colors indicating values more common in the ensemble.

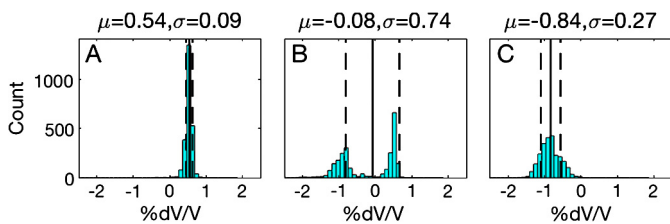


Fig. 6. Example of model distribution across a hemisphere boundary. Points A, B and C are indicated on Fig. 4 (a). Histograms at points A and C show single peaks of high and low velocity in the eastern and western hemispheres, respectively. At point B, the ensemble places some models in the East and some in the West, indicating a degree of uncertainty in the location of the boundary.

about whether the large standard deviations are due to uncertainty in the data or the boundaries can be resolved by examining the posterior pdf (e.g. Fig. 5). Fig. 6 gives another example of this. Histogram A shows the model values at point A in the eastern hemisphere and the Histogram C shows values for point C in the western hemisphere. Each is a roughly normal distribution around the mean value for that hemisphere. At the hemisphere boundary, Histogram B has a peak at each value, suggesting that the ensemble disagrees about which hemisphere point B is within.

The ensemble solution allows us to estimate the likelihood of finding a boundary transition at a given location. Fig. 7 shows the mean magnitude of the longitudinal gradient in the ensemble models, focusing on the two boundary locations. The Pacific boundary sits at 194°E above 30°N , but appears to bifurcate to

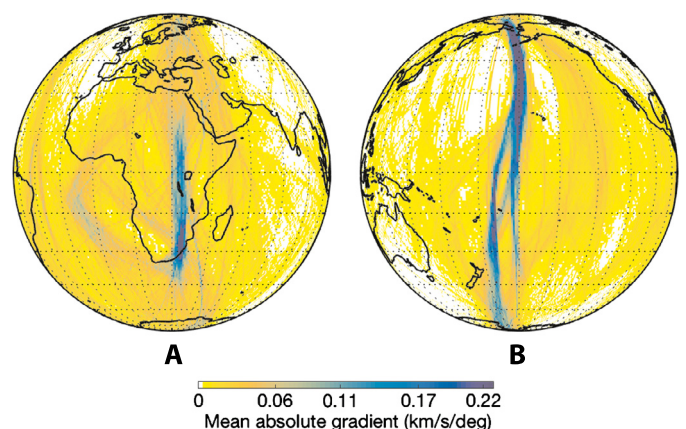


Fig. 7. Mean of absolute value of the longitudinal rate of change of isotropic V_p in the TBI model ensemble, centered on interpreted hemisphere boundaries. High values indicate locations of high longitudinal gradients in isotropic V_p .

the south. Towards the south, the boundary veers to $\sim 182^\circ$, while the other peak represents the addition of the lower velocity region within the western hemisphere. The boundary beneath Africa is centered around 28°E , but its uncertainty is greater and its location becomes very poorly constrained away from the equator.

The 2D TBI model favors regional variations in anisotropy that do not exhibit a hemispheric or global signature (Fig. 4b). Resolution tests suggest that, if present, our study would be able to

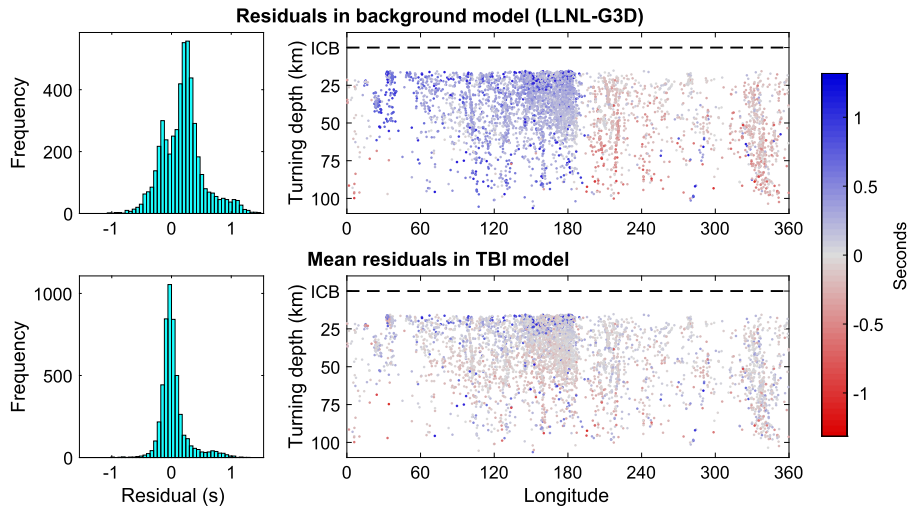


Fig. 8. Left: Histograms of *PKiKP-PKiKP* residuals in background (top) and preferred TBI model (bottom). Right: Residuals plotted with respect to turning point depth and longitude in the background model (top) and TBI model (bottom). TBI models produce an average of 58.9% variance reduction.

detect hemispheric variations in anisotropy (Figs. S12, S10). At high latitudes, the posterior distribution of the anisotropic terms is as broad as the proposal distribution, suggesting that available data does not improve estimates of axial anisotropy in those regions, reflecting the fact that rays travel almost entirely in the equatorial direction near the poles. Elsewhere in the model, the anisotropic variations rarely exceed 2σ . The most robustly determined region of anisotropy is beneath Africa, where $b + c$ reaches a maximum of 2.2% dV/V .

Fig. 4e visualizes the correlation between the isotropic perturbations and $b + c$. The model generally co-varies negatively throughout the inner core—when the isotropic velocity increases, $b + c$ decreases. This is due to the ray geometry and the geometry of anisotropy. In the absence of variation in ζ of raypaths in a region, there is a linear trade-off between dV , b , and c . The strongest correlation is around the hemisphere boundaries, suggesting there is also a trade-off between boundary location and the strength of anisotropy. Synthetic tests (Figs. S2, S6) suggest that this correlation could give rise to artificial structure in $b + c$, though at a significantly lower amplitude than the structure we recover here.

The ensemble models reduce the variance in the differential travel time residuals by an average of 58.9%, an improvement over the simpler quasi-hemisphere model (50.8% reduction). The residuals before and after the inversion are shown in Fig. 8. The coherent hemispheric pattern seen in the raw data has been removed, but a strong, un-modeled depth variation persists in the eastern hemisphere.

4. Discussion

4.1. Effect of 3D mantle structure

In order to estimate the effects of 3D mantle heterogeneity on the inferred inner core structure, we calculate rays and travel times in three Earth models: the 1D reference Earth model, AK135, and two 3D P-wave models. The first, the P-wave velocity model of Moulik and Ekstrom (2016) (ME2016), constrained in the lower mantle primarily by normal modes and low-frequency body wave travel-times, exhibits strong ($\pm 4\%$), long wavelength heterogeneity near the CMB. The second model, LLNL-G3Dv3 (Simmons et al., 2012) was created incorporating high-frequency body wave travel times and has shorter wavelength variations with smaller amplitudes ($\pm 2\%$ near CMB). These differences could potentially affect the retrieval of inner core structure, by, for example, changing

the calculated turning depth of *PKiKP* in the inner core. We find changes of turning depth on the order of 1 km due to 3D mantle heterogeneity, but the effect of geoidal versus spherical models is larger. For LLNL-G3Dv3, rays were traced in an oblate spheroidal Earth, resulting in a ~ 3 km difference in the radius of the ICB between the poles and equator. This difference has a minor effect on the length of inner core ray paths, but a pronounced effect on turning point (± 6 km depth below ICB). Since we calculate structure across a single layer this does not have consequences for our results presented here. However, this finding has implications for the proposed lateral shift in hemisphere boundaries with depth in the inner core (Waszek et al., 2011), as well as any other depth-varying structure (e.g. anisotropy).

Fig. 9 shows the effect of 3D mantle models on the predicted *PKiKP-PKiKP* times. The maps show the difference between differential times calculated in 3D (dT_{3D}) and 1D, AK135 (dT_{1D}) models, projected onto the core paths; the differences are summarized in histograms below. In the map, red indicates where the predicted differential travel times are smaller in the 3D models, which would lead to an interpretation of faster velocity in the inner core. Overall, effect of propagation through ME2016 is ± 0.1 s, and increases variance by $\sim 1\%$. Propagation through LLNL-G3Dv3 results in a median decrease of 0.18 s to the predicted times due to the fact that its uppermost inner core velocity is $\sim 0.4\%$ lower than in AK135. Correcting for this, effects of the mantle structure are ± 0.12 s and decrease variance by $\sim 6\%$. LLNL-G3Dv3 likely generates a larger effect than ME2016 due to shorter lengthscale variations in velocity.

Since observed residuals fall between ± 1.2 s, it is clear that mantle heterogeneity is not responsible for the majority of variations in the differential travel times. Indeed, 3D mantle structure choices do not manifest in any broad regional patterns, except around the large low shear velocity provinces beneath Africa and the Pacific Ocean. Even there, the estimated corrections have a total range of only 0.25 s, which falls within the scatter of the data, and consequently have limited effect on the features detected. This insensitivity to mantle structure is attributed to the close ray paths of *PKiKP* and *PKiKP* in the mantle. Mantle corrections will become more important for deeper-turning *PKiKP* rays (used in combination with *PKPab* or *PKPbc*, or absolute *PKiKP* measurements with no reference phase).

A comparison of the results using the three different mantle models is given in Fig. 10. Apart from minor details, the character of the mean models and their uncertainty for both isotropic and

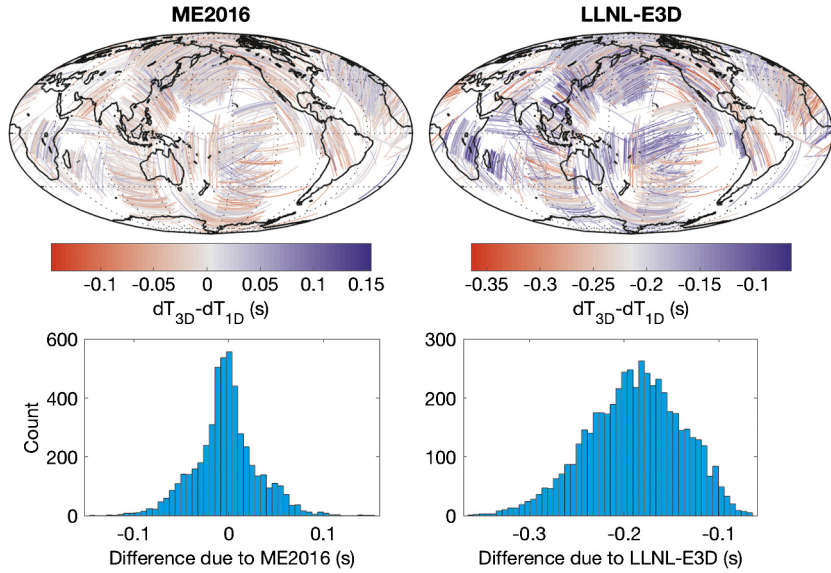


Fig. 9. Core paths (top) and histograms (bottom) of differential PKiKP-PKIKP times accrued in the mantle as predicted by two different mantle tomographic models, ME2016 and LLNL-E3D. Higher values translate into higher interpreted inner core velocity.

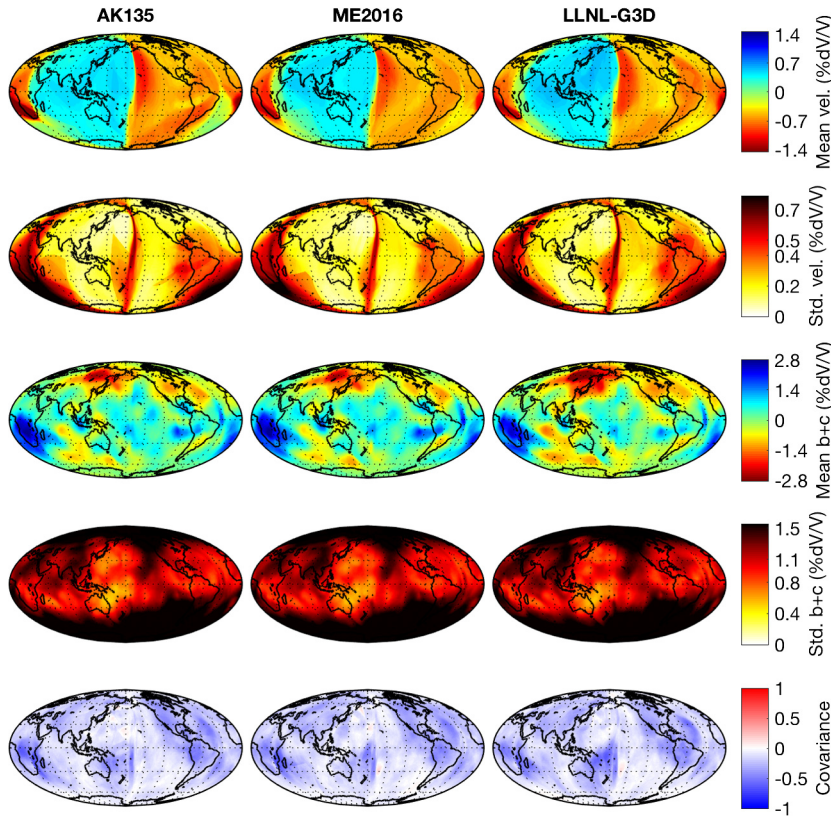


Fig. 10. Comparison of 2-D TBI ensemble models obtained using different background mantle models. Left: ak135, Middle: ME2016, Right: LLNL-G3D. (Row 1) Mean isotropic V_p . (Row 2) Standard deviation of isotropic V_p . (Row 3) Mean $b+c$ anisotropy. (Row 4) Standard deviation of $b+c$ terms. (Row 5) Posterior correlation between lateral variations of isotropic V_p and $b+c$.

anisotropic variations is essentially identical. The variance reduction in the three models is also similar. The AK135 model reduced variance by 58.5%, the ME3D model by 57.6% and the LLNL-G3Dv3 model by 58.9% (compared to predictions in AK135). The most visible difference between the models is the low isotropic perturbation present in the AK135 model below the southern Atlantic, is less prevalent in the other two. It also features slightly higher isotropic values in the Eastern hemisphere and a stronger $b+c$ anomaly beneath Siberia.

4.2. Regional-scale structure

Our tomographic model reveals evidence for regional variations in inner core velocity and anisotropy (Fig. 4). These variations are especially prominent in the pattern of anisotropy. By comparing regional variations against a range of potential model values – as shown in Fig. 5 – we can assess their robustness, accounting for both geographical and angular coverage. For example, like Pejić et al. (2017), we find that the sparse ray paths beneath South Amer-

ica and the Southern Atlantic Ocean preclude interpretations of model values in this region.

Regions of high positive velocity anisotropy beneath Africa and the Pacific Ocean (Fig. 4b, bc3) contrast with negative anisotropy detected beneath Siberia (bc1) and the North Atlantic Ocean (bc2). Regional anisotropy variations have previously been detected in body waves, particularly beneath the Pacific Ocean (Cormier et al., 2011; Irving and Deuss, 2015; Yu et al., 2017; Godwin et al., 2018), Africa (Yu and Wen, 2007; Irving, 2016), and Central America (Blom et al., 2015).

The regional scale structure does not display significant correlation with the hemispherical dichotomy, ruling out large-scale mechanisms as the source of anisotropy. While this precludes a better understanding of the origin of the hemispheres, it also indicates that there are likely multiple geodynamic processes which generate the inner core structures. For example, regional melting and freezing of the inner core boundary (Gubbins et al., 2011) could generate the observed regional structures. More rapid freezing would result in an increased lighter element content, which increases seismic velocity via a density decrease (Antonangeli et al., 2010). Melting would remove this light element content, with a corresponding velocity reduction. Other regional-scale processes include alignment to heat flow or magnetic field stresses (Karato, 1993; Bergman, 1997; Karato, 1999).

Despite the lack of hemispheric dichotomy in the anisotropic structure, we note that the extrema in anisotropic values are smaller for the western hemisphere. This may result from averaging over the isotropic upper layer here, which has previously been estimated with this dataset to extend to approximately 60 km below the inner core boundary (Waszek and Deuss, 2011). At present, our dataset and parametrization unable to constrain the potential effects of depth variation in anisotropy. The regional nature of the anisotropy also rules out a translation-induced mechanism for anisotropy in the inner core, whereby annealing during eastward translation produces weaker anisotropy in the eastern hemisphere (Bergman et al., 2010). Local maxima in anisotropy are located beneath Central and northern South America (Fig. 4b, bc4), which corresponds to data from the South Sandwich Islands generally used to infer strong anisotropy in the western hemisphere (Tkalčić, 2015; Blom et al., 2015). Our observations indicate that this region is in fact not representative of the upper western hemisphere structure.

4.3. Location and uncertainty of hemisphere boundaries

We find a trade-off between the location of hemisphere boundaries and the strength of anisotropy. This is particularly true for the boundary beneath Africa. The addition of cylindrical anisotropy moved the boundary location from 11° to 14° in the quasi-hemisphere model, while the 2D inversion further moved the average boundary longitude to $\sim 24^\circ$. These locations are within the bounds of those found by simple travel time analysis (Waszek et al., 2011). Recent regional work by Irving and Deuss (2015), Irving (2016) examining the boundary regions found similarly that the isotropic and anisotropic boundaries do not coincide, consistent with the interpretation that the hemispherical dichotomy characterizes isotropic velocity only.

For the isotropic hemisphere boundaries, the latitudinal variation we detect has been noted in recent studies (Irving and Deuss, 2015; Irving, 2016; Yu et al., 2017; Godwin et al., 2018), and our observations (Fig. 7) here are generally in excellent agreement. Some of the latitude variation (and uncertainty) in the location of boundaries may be due to depth dependent changes caused by the rotation of the inner core as it solidifies (Aubert et al., 2008; Waszek et al., 2011). Our tomographic inversion treats the uppermost inner core as a single layer and cannot constrain the variation

of boundary location with depth. However, Lasbleis et al. (2017) argues that such a depth shift cannot be constrained within errors for body waves, leading us to conclude that this effect is small in our models.

4.4. Trade-offs between isotropic and anisotropic variations

In the tomographic inversion presented here, regional-scale anisotropic variations tend to be larger in amplitude than the isotropic variations. This admits at least two different explanations: Processes that cause anisotropy indeed dominate the inner core, such as regional-scale heat flow or stresses (e.g. Karato, 1993; Bergman, 1997; Karato, 1999) which are stronger than the large-scale hemispherical growth processes (e.g. Aubert et al., 2008; Alboussière et al., 2010; Monnereau et al., 2010); Alternatively, axial anisotropy is not adequate for explaining the observed directional dependence of the travel times (Lythgoe and Deuss, 2015). Previously, Cormier et al. (2011) proposed that faster solidification in the east hemisphere could generate radial anisotropy, while slower freezing in the west hemisphere resulted in orientations parallel to the inner core boundary. A combination of these processes, with regional variation in the direction of the anisotropy parallel to the inner core boundary, could account for variations revealed by our tomographic model.

Our tomographic models shows that corrections for 3D mantle structure and geoid shape do not entirely account for the directional dependence of differential travel time observed in high latitude regions such as Siberia. Near the poles, *PKIKP* phases traverse the uppermost inner core travel almost entirely in the equatorial direction. When strong directional dependence is detected at high latitudes, it can only be explained by dubiously large (though mineralogically admissible) amounts of axial anisotropy (see Romanowicz et al., 2016 for table of compiled mineral physics values). A more parsimonious explanation for the observations might be azimuthal anisotropy or an axis of anisotropy tilted away from the rotational axis, as proposed in some regional studies (Creager, 1992; McSweeney et al., 1997). A full exploration of these possibilities could form the foundation for future studies.

5. Conclusions

We present a new tomographic study of both global and regional-scale structure of the uppermost inner core, including both isotropic and anisotropic velocity variations. The probabilistic and naturally parsimonious approach we use is well suited to inner core tomography, enabling us to retrieve hemisphere-size variations simultaneously with strong lateral jumps in isotropic velocity and small-scale structure where required by the data. By analyzing the properties of the resulting model ensembles, we come to the following notable conclusions:

- We find robust isotropic hemispheres (averages of 0.4% dV/V and -0.6% dV/V in the eastern and western hemispheres), with stronger regional variations in the western hemisphere ($\pm 0.3\%$ dV/V) than in the east. Isotropic velocity has a standard deviation of $\sigma \approx 0.2\%$ dV/V in well-resolved parts of the hemispheres, with larger uncertainty around South America and the Atlantic. Large standard deviations around the hemisphere boundaries are due to uncertainty in boundary location.
- We detect no corresponding hemispheric dichotomy in cylindrical anisotropy, assuming that its fast axis is aligned with the Earth's rotational axis. Robust detection of anisotropy is confined to areas where adequate crossing paths exist (beneath Africa and the eastern Pacific), and the uncertainty is everywhere higher than $\sigma = 0.6\%$ dV/V. Limited ray paths in

the axial direction lead to near-complete lack of constraint on anisotropy at latitudes greater than 45°.

- Analysis of the changeover between high and low isotropic velocity regions allows us to estimate the locations and uncertainty of hemisphere boundaries. We find the Pacific boundary varies by about 15° from north to south. Although the African boundary shows less variation, it is only constrained from 60°S to 30°N, beyond which there is little agreement in the model ensemble.
- We estimate that the effects of 3D mantle heterogeneity on our model of the inner core is minimal. Results found using 1D versus 3D reference models show little difference in anisotropic properties and their uncertainty, with minor differences to the isotropic velocity in the southern Atlantic. The deflection of the turning depth based on ray tracing in a reference geoid vs. a spherical Earth model may have implications that are not captured in our single-layer model.
- Regions of negative $b + c$ at high latitudes contradict mineralogical constraints on seismic anisotropy, suggesting cylindrical anisotropy may not be adequate for explaining body wave observations sensitive to the uppermost inner core.

Acknowledgements

S.B. acknowledges support from the NSF (EAR-1349771). L.W. is the recipient of a Discovery Early Career Research Award (project number DE170100329) funded by the Australian Research Council. V.L. acknowledges support from the National Science Foundation (CAREER grant EAR1352214) and from the Packard Fellowship for Science and Technology.

Appendix A. Supplementary material

Supplementary material related to this article can be found online at <https://doi.org/10.1016/j.epsl.2019.115789>.

References

- Agostinetti, N.P., Malinverno, A., 2010. Receiver function inversion by transdimensional Monte Carlo sampling. *Geophys. J. Int.* 181 (2), 858–872. <https://doi.org/10.1111/j.1365-246X.2010.04530.x>.
- Alboussi re, T., Deguen, R., Melzani, M., 2010. Melting-induced stratification above the Earth's inner core due to convective translation. *Nature* 466, 744–747.
- Antonangeli, D., Siebert, J., Badro, J., Farber, D., Fiquet, G., Morard, G., Ryerson, F., 2010. Composition of the Earth's inner core from high-pressure sound velocity measurements in Fe-Ni-Si alloys. *Earth Planet. Sci. Lett.* 295, 292–296.
- Aubert, J., Amit, H., Hulot, G., Olson, P., 2008. Thermochemical flows couple the Earth's inner core growth to mantle heterogeneity. *Nature* 454, 758–762.
- Bergman, M., 1997. Measurements of electric anisotropy due to solidification texturing and the implications for the Earth's inner core. *Nature* 389, 60–63.
- Bergman, M., Lewis, D., Myint, I., Slivka, L., Karato, S., Abreu, A., 2010. Grain growth and loss of texture during annealing of alloys, and the translation of Earth's inner core. *Geophys. Res. Lett.* 37.
- Blom, N., Deuss, A., Paulssen, H., Waszek, L., 2015. Inner core structure behind the PKP core phase triplication. *Geophys. J. Int.* 201, 1657–1665.
- Bodin, T., Sambridge, M., 2009. Seismic tomography with the reversible jump algorithm. *Geophys. J. Int.* 178 (3), 1411–1436.
- Bodin, T., Sambridge, M., Rawlinson, N., Arroucau, P., 2012. Transdimensional tomography with unknown data noise. *Geophys. J. Int.* 189 (3), 1536–1556.
- Burdick, S., Lekic, V., 2017. Velocity variations and uncertainty from transdimensional P-wave tomography of North America. *Geophys. J. Int.* 209, 1337–1351.
- Cao, A., Romanowicz, B., 2004. Hemispherical transition of seismic attenuation at the top of the Earth's inner core. *Earth Planet. Sci. Lett.* 228 (3–4), 243–253.
- Cormier, V., Attanayake, J., He, K., 2011. Inner core freezing and melting: constraints from seismic body waves. *Phys. Earth Planet. Inter.* 188, 163–172.
- Creager, K., 1992. Anisotropy of the inner core from differential travel times of the phases PKP and PKIKP. *Nature* 356, 309–314.
- Creager, K., 1999. Large-scale variations in inner core anisotropy. *J. Geophys. Res.* 104, 23127–23139.
- Crotwell, H., Owens, T., Ritsema, J., 1999. The TauP toolkit: flexible seismic travel-time and raypath utilities. *Seismol. Res. Lett.* 70, 154–160.
- Deguen, R., Alboussi re, T., Cardin, P., 2013. Thermal convection in Earth's inner core with phase change at its boundary. *Geophys. J. Int.* 193, 1310–1334.
- Deuss, A., Irving, J., Woodhouse, J., 2010. Regional variation of inner core anisotropy from seismic normal mode observations. *Science* 328, 1018–1020.
- Gao, C., Lekic, V., 2018. Consequences of parametrization choices in surface wave inversion: insights from transdimensional Bayesian methods. *Geophys. J. Int.* 215 (2), 1037–1063. <http://dx.doi.org/10.1093/gji/ggy310>.
- Garcia, R., Souriau, A., 2000. Inner core anisotropy and heterogeneity level. *Geophys. Res. Lett.* 27, 3121–3124.
- Geballe, Z., Lasbelis, M., Cormier, V., Day, E., 2013. Sharp hemisphere boundaries in a translating inner core. *Geophys. Res. Lett.* 40, 1719–1723.
- Godwin, H., Waszek, L., Deuss, A., 2018. Measuring the seismic velocity in the top 15 km of Earth's inner core. *Phys. Earth Planet. Inter.* 274, 158–169.
- Green, P.J., 1995. Reversible jump Markov chain Monte Carlo computation and Bayesian model determination. *Biometrika* 82 (4), 711–732.
- Gubbins, D., Sreenivasan, B., Mound, J., Rost, S., 2011. Melting of the Earth's inner core. *Nature* 473, 361–363.
- Irving, J., 2016. Imaging the inner core under Africa and Europe. *Phys. Earth Planet. Inter.* 254, 12–24.
- Irving, J., Deuss, A., 2011. Hemispherical structure in inner core velocity anisotropy. *J. Geophys. Res.* 116, 4307–4323.
- Irving, J., Deuss, A., 2015. Regional seismic variations in the inner core under the North Pacific. *Geophys. J. Int.* 203, 2189–2199.
- Karato, S., 1993. Inner core anisotropy due to the magnetic field-induced preferred orientation of iron. *Science* 262, 1708–1711.
- Karato, S., 1999. Seismic anisotropy of the Earth's inner core resulting from flow induced by Maxwell stresses. *Nature* 402, 871–873.
- Kennett, B., Engdahl, E., Buland, R., 1995. Constraints on seismic velocities in the Earth from travel times. *Geophys. J. Int.* 122, 108–124.
- Kolb, J.M., Lekic, V., 2014. Receiver function deconvolution using transdimensional hierarchical Bayesian inference. *Geophys. J. Int.* 197 (3), 1719–1735.
- Lasbleis, M., Waszek, L., Day, E., 2017. GrowYourIC: a step towards a coherent model of seismic structure. *Geochem. Geophys. Geosyst.* 18, 4016–4026.
- Lythgoe, K., Deuss, A., 2015. The existence of radial anisotropy in Earth's upper inner core revealed from seismic normal mode observations. *Geophys. Res. Lett.* 42, 4841–4848.
- Malinverno, A., 2002. Parsimonious Bayesian Markov chain Monte Carlo inversion in a nonlinear geophysical problem. *Geophys. J. Int.* 151 (3), 675–688.
- McSweeney, T., Creager, K., Merrill, R., 1997. Depth extent of inner-core seismic anisotropy and implications for geomagnetism. *Phys. Earth Planet. Inter.* 101, 131–156.
- Metropolis, N., Rosenbluth, A.W., Rosenbluth, M.N., Teller, A.H., Teller, E., 1953. Equation of state calculations by fast computing machines. *J. Chem. Phys.* 21 (6), 1087–1092.
- Monnerieu, M., Calvet, M., Margerin, L., Souriau, A., 2010. Lopsided growth of Earth's inner core. *Science* 328, 1014–1017.
- Morelli, A., Dziewoński, A., Woodhouse, J., 1986. Anisotropy of the inner core inferred from PKIKP travel times. *Geophys. Res. Lett.* 13, 1545–1548.
- Moulik, P., Ekstrom, G., 2016. The relationships between large-scale variations in shear velocity, density, and compressional velocity in the Earth's mantle. *J. Geophys. Res., Solid Earth* 121 (4), 2737–2771.
- Niu, F., Wen, L., 2001. Hemispherical variations in seismic velocity at the top of the Earth's inner core. *Nature* 410, 1081–1084.
- Okabe, A., Boots, B., Sugihara, K., 1992. *Spacial Tessellations: Concepts and Applications of Voronoi Diagrams*. John Wiley & Sons Inc., New York, NY.
- Olugboji, T.M., Lekic, V., McDonough, W., 2017. A statistical assessment of seismic models of the US continental crust using Bayesian inversion of ambient noise surface wave dispersion data. *Tectonics* 36 (7), 1232–1253.
- Peji c, T., Tkal c, H., Sambridge, M., Cormier, V., Benavente, R., 2017. Attenuation tomography of the upper inner core. *J. Geophys. Res.* 122, 3008–3032.
- Piana Agostinetti, N., Giacomuzzi, G., Malinverno, A., 2015. Local three-dimensional earthquake tomography by trans-dimensional Monte Carlo sampling. *Geophys. J. Int.* 201 (3), 1598–1617.
- Pozzo, M., Davies, C., Gubbins, D., Alf e, D., 2012. Thermal and electrical conductivity of iron at Earth's core conditions. *Nature* 485, 355–358.
- Romanowicz, B., Cao, A., Godwal, B., Wenk, R., Ventosa, S., Jeanloz, R., 2016. Seismic anisotropy in the Earth's innermost inner core: testing structural models against mineral physics predictions. *Geophys. Res. Lett.* 43, 93–100.
- Sambridge, M., Gallagher, K., Jackson, A., Rickwood, P., 2006. Trans-dimensional inverse problems, model comparison and the evidence. *Geophys. J. Int.* 167 (2), 528–542.
- Simmons, N.A., Myers, S.C., Johannesson, G., Matzel, E., 2012. LLNL-G3Dv3: global P wave tomography model for improved regional and teleseismic travel time prediction. *J. Geophys. Res., Solid Earth* 117 (B10).
- Song, X., Helmberger, D., 1995. Depth dependence of anisotropy of Earth's inner core. *J. Geophys. Res.* 100, 9805–9816.
- Tanaka, S., Hamaguchi, H., 1997. Degree one heterogeneity and hemispherical variation of anisotropy in the inner core from PKP(BC) - PKP(DF) times. *J. Geophys. Res.* 102, 2925–2938.
- Tkal c, H., 2015. Complex inner core of the Earth: the last frontier of global seismology. *Rev. Geophys.* 53, 59–94.
- Tkal c, H., Young, M., Muir, J.B., Davies, D.R., Mattesini, M., 2015. Strong, multi-scale heterogeneity in Earth's lowermost mantle. *Sci. Rep.* 5, 18416.

- Waszek, L., Deuss, A., 2011. Distinct layering in the hemispherical seismic velocity structure of Earth's upper inner core. *J. Geophys. Res.* 116, 12313–12326.
- Waszek, L., Deuss, A., 2013. A low attenuation layer in Earth's uppermost inner core. *Geophys. J. Int.* 195, 2005–2015.
- Waszek, L., Irving, J., Deuss, A., 2011. Reconciling the hemispherical structure of Earth's inner core with its super-rotation. *Nat. Geosci.* 4, 264–267.
- Woodhouse, J., Giardini, D., Li, X., 1986. Evidence for inner core anisotropy from free oscillations. *Geophys. Res. Lett.* 13, 1549–1552.
- Young, M.K., Tkalcic, H., Bodin, T., Sambridge, M., 2013. Global P wave tomography of Earth's lowermost mantle from partition modeling. *J. Geophys. Res., Solid Earth* 118 (10), 5467–5486.
- Yu, W., Su, J., Song, T., Huang, H., Mozziconacci, L., Huang, B., 2017. The inner core hemispheric boundary near 180°W. *Phys. Earth Planet. Inter.* 272, 1–16.
- Yu, W., Wen, L., 2007. Complex seismic anisotropy in the top of the Earth's inner core beneath Africa. *J. Geophys. Res.* 112, 8304–8321.